

Sustainable Salt Template-Assisted Chemical Activation for the Production of Porous Carbons with Enhanced Power Handling Ability in Supercapacitors

Noel Díez,^[a] Guillermo A. Ferrero,^[a] Antonio B. Fuertes,^[a] and Marta Sevilla*^[a]

Highly porous materials with a 3D framework have been produced by a sustainable salt template-assisted chemical activation approach based on the use of KCl particles as template, K_2CO_3 particles as both template and activating agent, and biomass-derivatives as carbon precursor (i.e., glucose and soybean meal). The self-assembly of all the constituents into a 3D structure is achieved by a freeze-drying process. After carbonization and a simple washing step with water, a 3D hierarchical porous carbon is obtained. The sustainability of the

process is ensured by using chemicals of low or null toxicity and renewable carbon precursors. The materials produced are characterized by a 3D framework composed of thin walls rich in micropores, with BET surface areas in excess of $2000\text{ m}^2\text{ g}^{-1}$ and pore volumes of up to $1.4\text{ cm}^3\text{ g}^{-1}$. These materials show an improved rate capability in supercapacitors based on aqueous (H_2SO_4 and Li_2SO_4) and ionic liquid electrolytes (EMImTFSI/AN) with carbon electrode loadings well within the range of commercial values.

1. Introduction

Nanoporous carbon materials are a key ingredient of many energy-related technologies, such as supercapacitors,^[1–3] Li-ion batteries (particularly Li–S/Li–Se/Li–air batteries),^[4–7] fuel cells,^[8,9] hydrogen/methane storage^[10,11] and carbon capture systems.^[12,13] This is due to their excellent properties, such as their large specific surface area, low density, good electronic conductivity, high thermal stability and tunable chemical properties. There is, therefore, a growing demand for such materials, which needs to be satisfied without compromising either resources or the environment. This is why biomass is one of the preferred carbon precursors for the production of high-performance, sustainable porous carbons.^[14,15] Other advantages of biomass and biomass residues include their widespread availability/natural abundance and low-cost. However, when biomass is carbonized directly, it normally produces carbons with insufficient or low porosity. Consequently, traditional activation approaches (i.e., chemical and physical activation) are implemented in order to produce highly porous carbons from biomass.^[16,17] This scenario has led in the last decade to an exponential exploitation of KOH as activating agent. However, although KOH has proven perfectly well that it can produce high-performance porous carbons for a wide variety of applications,^[18,19] its use for industrial purposes poses certain challenges, such as its high toxicity and corrosiveness. It also generates mainly micropores and in specific cases mesopores,^[20–22] but normally no macroporous hierarchical 3D structures (unless they are inherited from the biomass or

aggressive – and low yield – activation conditions are used).^[23] This kind of structure is advantageous for speeding up diffusion processes. In fact, the diffusion time is proportional to the square of the diffusion distance, which is within the nanometer range in these structures. This has led scientists to search for greener alternatives which, at the same time, favor the production of hierarchical porous carbons or 2D/3D porous carbon structures. For example, Deng *et al.* have shown that a benign potassium salt, such as potassium bicarbonate, is capable of producing 3D hierarchical porous carbons (surface areas of up to *ca.* $1900\text{ m}^2\text{ g}^{-1}$) from both biomass and biomass derivatives.^[24] Zhao's group developed 3D hierarchical porous carbons from glucose by combining multiscale inorganic salts ($NaCl$, Na_2CO_3 and Na_2SiO_3) and by controlling their crystallization and assembly through a freeze-drying process.^[25,26] In this approach, $NaCl$ particles served as template for the generation of macrocavities in the $1\text{--}2\text{ }\mu\text{m}$ range, Na_2CO_3 particles for the formation of macropores in the $50\text{--}100\text{ nm}$ range, and Na_2SiO_3 particles to generate mesopores in the $5\text{--}10\text{ nm}$ range, while the carbonization of glucose gave rise to some micropores. These materials had surface areas below $1100\text{ m}^2\text{ g}^{-1}$, although pore volumes of up to $1.5\text{ cm}^3\text{ g}^{-1}$ were achieved due to the abundance of large mesopores/small macropores. Besides Zhao's group, other authors have shown the efficient templating function of $NaCl$ crystals for the production of materials with a 3D macroporous framework^[27–31] or 2D nanosheets^[32,33] – depending on the preparation conditions –, by using various precursors (glucose, polypyrrole, sodium glutamate, citric acid or lysine). However, all of the produced materials possess a low micropore development (except in the case of sodium glutamate), which led to surface areas below $800\text{ m}^2\text{ g}^{-1}$. This limits, for example, the ion storage capacity of these materials for supercapacitor applications, which is mainly determined by micropores.^[1,34] On the other hand, Fellinger's group has revisited $ZnCl_2$ as chemical activating agent and used its low

[a] N. Díez, G. A. Ferrero, A. B. Fuertes, Dr. M. Sevilla
Instituto Nacional del Carbón (CSIC)
Francisco Pintado Fe, 26; Oviedo 33011, Spain
E-mail: martasev@incar.csic.es

 Supporting information for this article is available on the WWW under
<https://doi.org/10.1002/batt.201900037>

melting eutectic mixtures with several chloride salts (e.g. KCl, NaCl or LiCl) to produce hierarchical porous carbons with surface areas up to *ca.* 3000 m² g⁻¹.^[35–37] They have shown that when excess NaCl/KCl is used in this salt-templating strategy, the NaCl/KCl solid particles dispersed in the liquid reaction mixture can act as hard templates for macropores.^[36,37] A drawback in this strategy is the toxicity of ZnCl₂.

Herein, we propose a sustainable salt template-assisted chemical activation approach for the production of highly porous 3D carbons based on the use of KCl particles as template and K₂CO₃ particles as both template and activating agent. By means of a freeze-drying process, the KCl and K₂CO₃ particles self-assemble to form a 3D structure which is uniformly covered by the carbon precursor. The subsequent carbonization and removal of the template/activating agent then produces porous carbons with a 3D framework and surface areas in the 2000–2600 m² g⁻¹ range. Noteworthy, there is also a certain confinement effect produced by the presence of inert KCl particles, which slightly increases the product yield. The sustainability of the process is supported by the use of biomass derivatives (glucose) or biomass residues (soybean meal) as carbon precursor, and templates (KCl and K₂CO₃) and activating agents (K₂CO₃) which can be washed off by simply using water, without the need for any acid. When tested as supercapacitor electrodes using carbon loadings well within the range of commercial values, these materials showed an excellent performance at high current rates in a variety of electrolytes with different ionic conductivities.

2. Results and Discussion

2.1. Structural and Textural Properties of the 3D Sponge-Like Porous Carbons

The salt template-assisted chemical activation proposed herein is based on the use of KCl particles as template, and K₂CO₃ particles as template and activating agent (see Scheme 1).



Scheme 1. Synthesis procedure for obtaining 3D porous carbons.

When the solution formed with glucose or soybean meal is freeze-dried, KCl crystallizes into cubic and tubular particles in the micron range, whereas K₂CO₃ crystallizes into smaller particles (*vide infra*). Both kinds of particles self-assemble into a 3D structure and become covered by the carbon precursor, i.e., glucose or soybean meal (see Scheme 1). After carbonization, the KCl particles and un-reacted K₂CO₃ can be washed off by simply using water to ensure the sustainability of the process. The final result is a carbon material with a 3D sponge-like microporous structure, as illustrated in Scheme 1. The carbon materials produced from glucose are labelled as G-T and those from soybean meal as SM-T, where T is the synthesis temperature.

Figures S1a–b show SEM micrographs of the freeze-dried samples corresponding to glucose or soybean meal and KCl. They reveal that, under the freeze-drying process, KCl tends to form microparticles with a cubic and tubular shape, the size of the KCl particles being smaller (<2 μm) in the case of soybean meal compared to glucose (>2 μm). The particles are homogeneously covered by the carbon precursors as is evidenced by the corresponding EDX mappings (Figures S1c–f). Under the same conditions, K₂CO₃ forms smaller particles which agglomerate (Figures S2a–2b) and also become covered by the soybean carbon precursor, as confirmed by EDX nitrogen mapping (Figures S2c–2d), a precursor which under freeze-drying conditions tends to form lamellar structures (Figure S3). In the case of the freeze-dried samples produced from the combined mixture of KCl and K₂CO₃ with the corresponding carbon precursor, both kinds of structures self-assemble, although the KCl particles are more prominent owing to the fact that a much higher amount of KCl is used (Figure 1). In the case of soybean meal (Figures 1c–e), the uniform covering of the particles by the precursor is confirmed by nitrogen EDX mapping.

Figure 2 shows SEM micrographs of the carbon materials produced at 850 °C from glucose (Figures 2a and 2b) and soybean meal (Figures 2c and 2d) after the removal of KCl and un-reacted K₂CO₃ (SEM micrographs of the materials synthe-

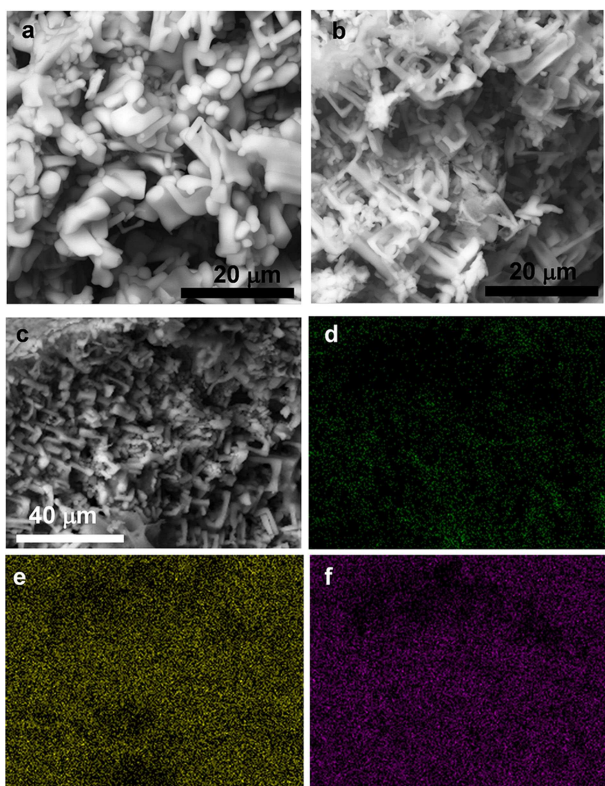


Figure 1. a) Freeze-dried mixture of glucose, KCl and K_2CO_3 , b) freeze-dried mixture of soybean meal, KCl and K_2CO_3 , and EDX mappings performed in the soybean meal-based mixture on the area shown in (c) for d) nitrogen, e) chlorine and f) potassium.

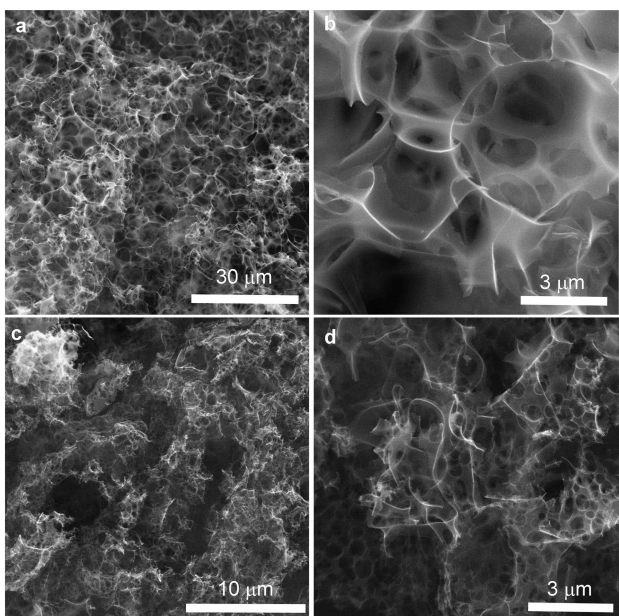


Figure 2. SEM micrographs of the carbon materials produced at 850 °C from the freeze-dried mixtures of KCl, K_2CO_3 and a, b) glucose (G-850), and c, d) soybean meal (SM-850).

sized at 800 °C can be seen in Figure S4). As can be seen from the micrographs, irrespective of the carbon precursor or the

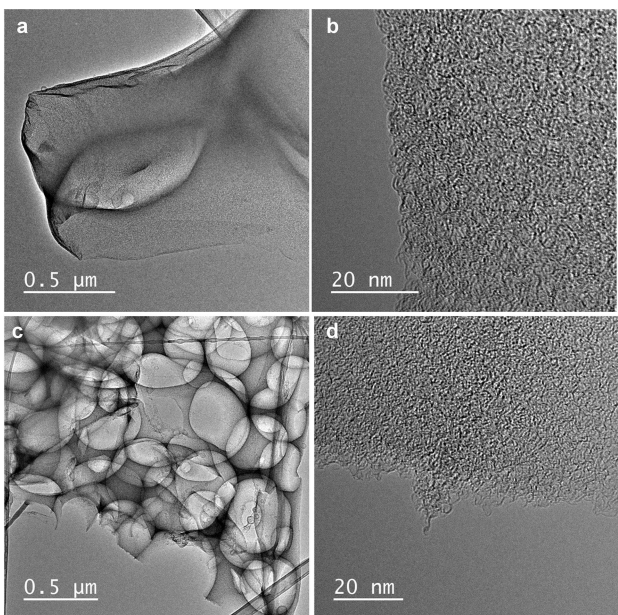


Figure 3. TEM/HRTEM micrographs of the carbon materials produced at 850 °C from the freeze-dried mixtures of KCl, K_2CO_3 and a), b) glucose (G-850), and c), d) soybean meal (SM-850).

synthesis temperature used, the resulting carbon materials have a 3D framework with very thin walls. This structure is confirmed by TEM analysis. Transparent, interconnected carbon sheets can be seen in the TEM micrographs in Figures 3a and 3c. Further magnification by HRTEM reveals an abundant and disordered microporosity within the walls (Figures 3b and 3d). Comparison of the structure of these materials with that of the carbons produced by using only K_2CO_3 (Figures S5a and S5b) or only KCl (Figures S5c and S5d) shows that it is the self-assemblage of KCl and K_2CO_3 particles that determines the final structure of the material.

Thermogravimetric analysis (TGA) and temperature programmed desorption (TPD) experiments of the mixtures of glucose or soybean meal and KCl + K_2CO_3 were performed in order to analyze the processes taking place. The corresponding TGA and DTG curves are depicted in Figures 4a–4d. Independently of the carbon precursor used, a sharp weight loss was recorded at temperatures higher than 700 °C, which is ascribed to the following redox reaction:^[38–40] $K_2CO_3 + 2 C \rightarrow 2 K + 3 CO$. In this way, carbon atoms are etched as CO, giving rise to microporosity (see N₂ physisorption analysis below). This reaction has been confirmed by TPD experiments. Thus, as shown in Figures 4e–4f, an intense CO evolution peak (highlighted in red) is registered above 600 °C, with a maximum at 760–780 °C. On the other hand, the carbonization of both precursors takes place at temperatures lower than 500 °C. When compared to the TGA/DTG curves of the pristine precursors, it can be seen that in both cases the main decomposition peaks are located at a temperature higher than in the mixture with KCl + K_2CO_3 . This can be attributed to the catalytic action of K_2CO_3 , as already observed in the case of other potassium salts such as KHCO₃^[24] or K₂C₂O₄.^[41] Indeed, the TPD experiments show intense CO₂ (highlighted in blue) and

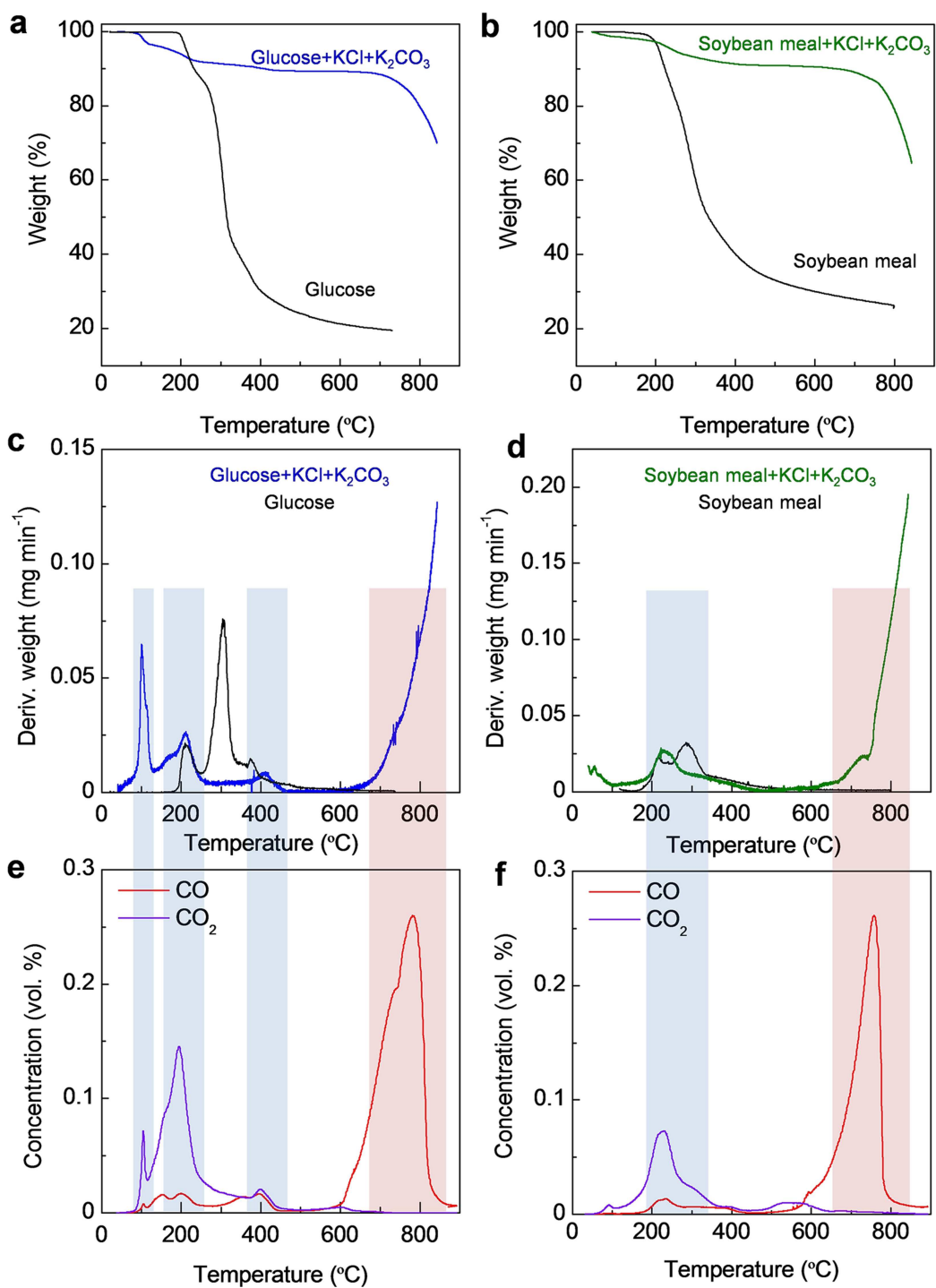


Figure 4. a) TGA, c) DTG and e) TPD curves of the freeze-dried mixture of glucose, KCl and K₂CO₃, b) TGA, d) DTG and f) TPD curves of the freeze-dried mixture of soybean meal, KCl and K₂CO₃ (heating rate: 3 °C min⁻¹, N₂ and Ar atmospheres for TGA and TPD experiments, respectively).

H₂O evolution peaks below 250 °C (see Figures 4e, 4f and S6) – with a smaller contribution from CO –, because of dehydration and polymerization reactions (the first H₂O evolution peak at ~60 °C in the case of soybean meal and the hump at ~70 °C in the first H₂O evolution peak corresponding to glucose may be ascribed to the presence of water adsorbed during handling). The weight loss at around 400–500 °C is associated with the

evolution of CO₂ (highlighted in blue) and of H₂ resulting from the continued carbonization of the precursors (see Figure S6).

X-ray diffraction was used to analyze the nature of the inorganic species present in the materials after the high temperature treatment and to corroborate the complete removal of these species by washing with water. Figure 5 shows the corresponding XRD patterns before and after washing with water. As can be seen in Figures 5a–b, KCl and

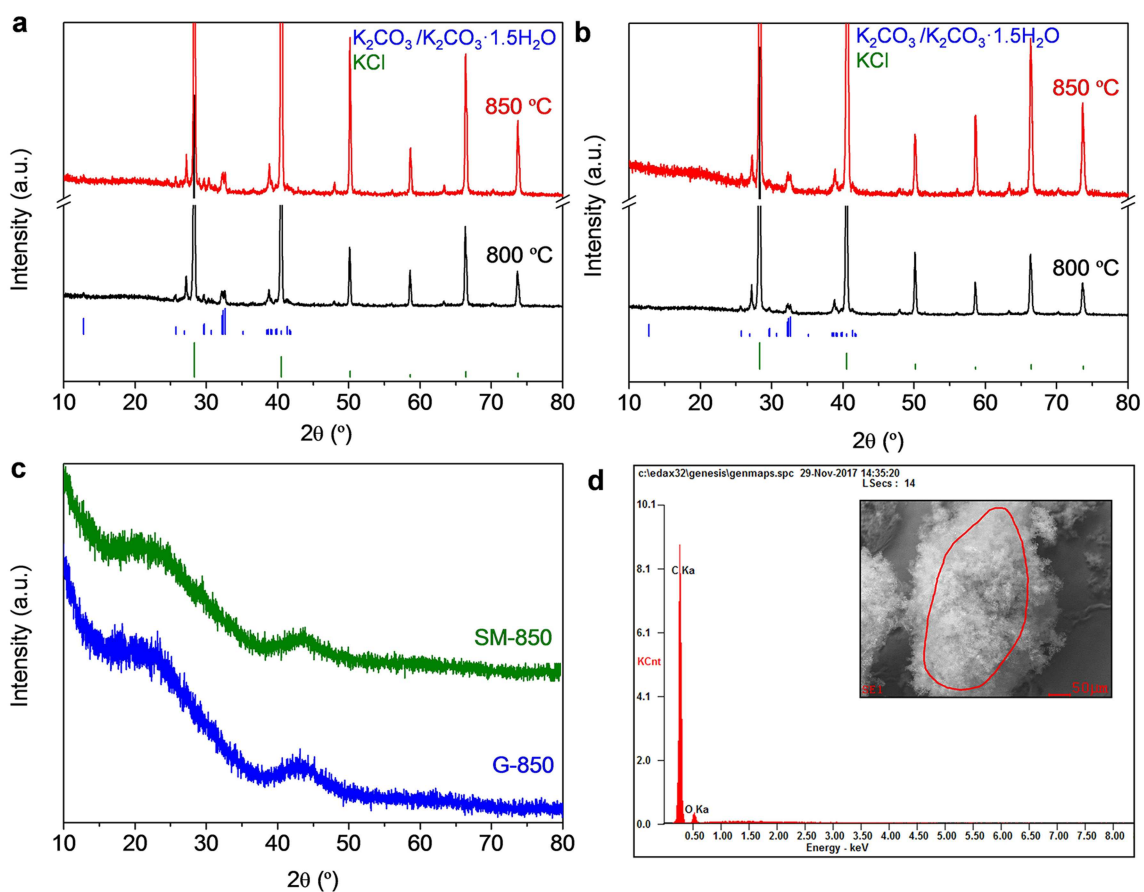


Figure 5. XRD patterns corresponding to the samples produced from the freeze-dried mixture of KCl, K₂CO₃ and a) glucose and b) soybean meal before washing, c) XRD patterns of the carbon materials after washing and d) EDX analysis of a carbon material after washing.

un-reacted K₂CO₃ are the only species remaining after the high temperature treatment. After washing with water (Figure 5c), no potassium salt remains, which is a significant advantage compared to hard templating^[42] or other activation approaches,^[23,24] which use acids such as HF or HCl. The complete removal of the potassium salts was corroborated by EDX analysis, as shown in Figure 5d. The XRD patterns of the carbon materials are of the type that is characteristic of activated carbons, i.e., materials with an amorphous structure, showing low intensity and broad (002) and (100) bands with a high-intensity tailing at 20~10°, which is indicative of the presence of abundant porosity.^[25,27,43–45]

Analysis of the porous structure of the carbon materials was performed by means of N₂ physisorption at -196°C. The corresponding isotherms and pore size distributions (PSDs) are shown in Figure 6. As revealed by Figures 6a and 6b, G-800 shows a Type I(a) isotherm which is typical of almost exclusively microporous materials, whereas G-850, SM-800 and SM-850 have a Type I(b) isotherm that is indicative of materials with a broad PSD including narrow mesopores (< ~2.5 nm).^[46] This is confirmed by the PSDs in Figures 6c and 6d. Thus, G-800 has virtually no pores above 2 nm, whereas the rest of the carbons possess pores in the 2.5–4 nm range. On the other hand, the increase in N₂ adsorption at relative pressures >0.9 indicates the presence of large mesopores/small macropores as a result

of the templating of small KCl/K₂CO₃ particles. This is particularly pronounced in the case of the materials derived from soybean meal and is in accordance with the smaller size of the template particles, as the SEM analysis shows (see above). The textural properties of the different carbon materials are collected in Table 1. All the materials have large BET surface areas, in the ~2000–2600 m² g⁻¹ range, and pore volumes in the range of 0.8–1.4 cm³ g⁻¹ (it should be noted that this pore volume has been calculated from the N₂ isotherms and, therefore, it does not include macropores), with most of this porosity corresponding to micropores (> 70%). Comparison with the materials prepared by using only KCl particles as template, which exhibit a poor pore development ($S_{\text{BET}} < 500 \text{ m}^2 \text{ g}^{-1}$ and $V_p < 0.4 \text{ cm}^3 \text{ g}^{-1}$) and a higher product yield (Table 1), evidences the activating (carbon etching) role of K₂CO₃. On the other hand, comparison with the materials prepared by using only K₂CO₃, shows that, in the case of glucose, the generation of porosity is more effective in this salt template-assisted chemical activation process (see Table 1). This may be related to the fact that, during the carbonization process and at $T > 631^\circ\text{C}$, KCl microparticles coexist with an eutectic mixture of KCl and K₂CO₃, and above 750 °C only this eutectic mixture is found (Figure S7).^[47,48] This salt melt does not affect the rigid 3D carbon framework already formed but facilitates the redox reaction that takes place at $T > 700^\circ\text{C}$.

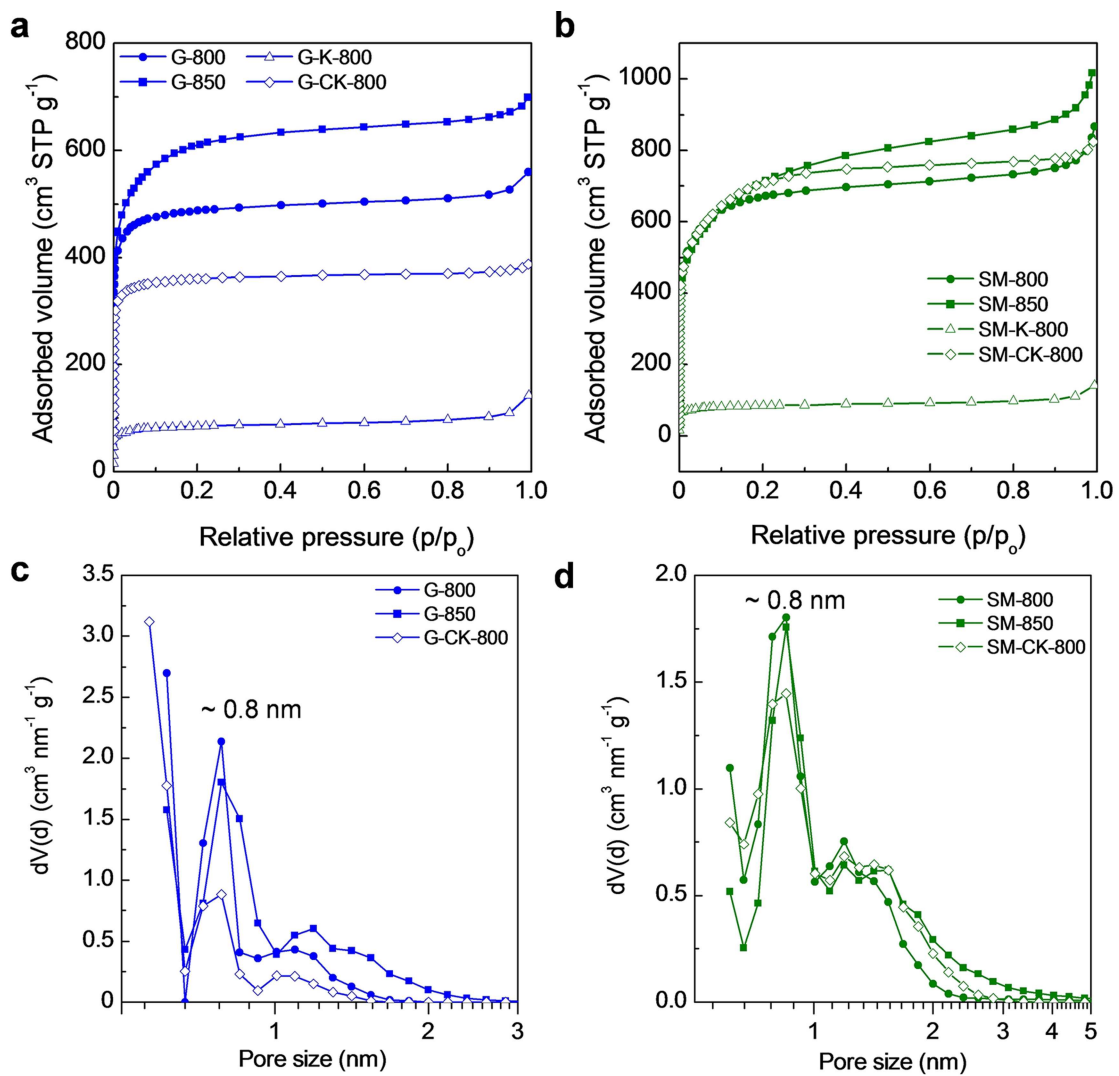


Figure 6. N₂ physisorption isotherms of the carbon materials produced from the freeze-dried mixture of KCl, K₂CO₃ and a) glucose and b) soybean meal, and the corresponding PSDs for the c) glucose-based carbons and d) soybean meal-based carbons.

Table 1. Physico-chemical properties of the porous carbons.

Carbon	Precursor	Activating/templating agent	Yield [%] ^a	Textural properties			Electrode packing density [g cm ⁻³] ^c
				S _{BET} [m ² g ⁻¹]	V _p [cm ³ g ⁻¹] ^b	V _{micro} [cm ³ g ⁻¹]	
SM-K-800	Soybean meal	KCl	17	470	0.38	0.16	–
SM-CK-800		K ₂ CO ₃	11	2650	1.22	1.04	–
SM-800		KCl + K ₂ CO ₃	13	2580	1.19	0.98	0.32
SM-850		KCl + K ₂ CO ₃	10	2613	1.42	1.00	0.25
G-K-800	Glucose	KCl	26	335	0.16	0.12	–
G-CK-800		K ₂ CO ₃	14	1443	0.58	0.53	–
G-800		KCl + K ₂ CO ₃	16	2000	0.81	0.71	0.59
G-850		KCl + K ₂ CO ₃	14	2316	1.04	0.90	0.42

^a Yield is defined as grams of carbon/grams of precursor × 100. ^b The total pore volume was determined at a P/P₀ of ~0.95. ^b The micropore volume was determined by using the QSDFT PSD. ^c Calculated by measuring the thickness of the electrodes with the help of a micrometer.

between K₂CO₃ and carbon (a solid-liquid reaction instead of a solid-solid), which leads to greater pore development. Similar results were obtained when potassium oxalate was employed instead of potassium carbonate. Glucose activated with potassium oxalate (1/1 wt. ratio) produces a material with a

surface area of 1280 m² g⁻¹ and a pore volume of 0.5 cm³ g⁻¹, whereas glucose activated with potassium oxalate in the presence of KCl (glucose/K₂C₂O₄/KCl = 1/1/6.7 wt. ratio) increases the surface area and pore volume up to 1750 m² g⁻¹ and 0.74 cm³ g⁻¹ respectively (see Figure S8). It is worth noting

that the materials derived from soybean meal have a larger pore development than those produced from glucose, with surface area values as high as $2600\text{ m}^2\text{ g}^{-1}$ (Table 1). This may be due to the preferential removal of nitrogen species – besides the etching of carbon atoms – when activating with potassium salts. Thereby, as shown by elemental analysis, almost all nitrogen is removed during the activation process (it decreases from 8.1 wt.% in soybean meal to ~0.4–0.5 wt.%), whereas during carbonization most of nitrogen is preserved (see Table S1). Also worth highlighting is the 2% increase registered in the product yield in this salt template-assisted chemical activation compared to the traditional chemical activation process (see Table 1), which can be attributed to the confinement effect produced by the presence of inert KCl particles, as we have recently shown for another activating agent such as sodium thiosulfate.^[49]

2.2. Electrochemical Properties of 3D Porous Carbons

The combination of a 3D morphology that provides short diffusion pathways with a large surface area ascribed mainly to micropores but also some small mesopores (<4 nm), and an electronic conductivity of $\sim 2\text{ S cm}^{-1}$ (measured for the compressed powder at 7 MPa), make these materials suitable for high power EDLC applications. The rich density of micropores provides a high ion storage capacity, while the 3D morphology provides rapid access to the pores, thereby ensuring retention of capacitance at high rates. Taken into account these considerations and in order to determine the full potential of these materials, their electrochemical properties were analyzed in three electrolytes with different ionic conductivities and able to stand different voltage windows: i) 1 M H_2SO_4 , ii) 1 M Li_2SO_4 and iii) EMImTFSI/AN. Symmetrical two-electrode cells were assembled using a carbon loading well within the range of commercial values, i.e., 9–11 mg cm^{-2} . The packing density of the electrodes ranges in the $0.25\text{--}0.59\text{ g cm}^{-3}$ range (vs. 0.68 g cm^{-3} for commercial activated carbons) (Table 1). It should be noted that tailoring of macroporosity should be performed for optimizing the volumetric performance.

When a solution of 1 M H_2SO_4 is used as electrolyte, all the materials provide a large specific capacitance at low rates, $\sim 220\text{--}240\text{ F g}^{-1}/50\text{--}112\text{ F cm}^{-3}$ (values which are within those of the state-of-the-art in carbon materials and superior to those of commercial activated carbons, $135\text{--}155\text{ F g}^{-1}/78\text{--}90\text{ F cm}^{-3}$)^[15,44,50] and are still able to retain above 100 F g^{-1} (~30–40 F cm^{-3}) at ultra-large currents of $80\text{--}110\text{ A g}^{-1}$ (see Figure 7a). At 0.2 A g^{-1} , the surface area normalized capacitance increases following the trend of microporosity, i.e., G-800 ($11.2\text{ }\mu\text{F cm}^{-2}$)>G-850 ($9.8\text{ }\mu\text{F cm}^{-2}$)>SM-800 ($9.4\text{ }\mu\text{F cm}^{-2}$)>SM-850 ($9.0\text{ }\mu\text{F cm}^{-2}$), all of these values being within the theoretical EDLC surface area normalized capacitance of carbon materials.^[51] The excellent rate performance provided by the 3D morphology – despite using thick electrodes – is also confirmed by the moderate drop in voltage in the charge/discharge experiments at very high rates (see Figure S9) and also by the well-preserved rectangular CVs at high scan rates (Figure S10).

On the other hand, a study of the ion-dynamics through EIS (Figure 8a) shows that the better rate capability of the materials prepared at higher temperature (850°C) is due to their higher electronic conductivity (lower ESR). Meanwhile, the better rate capability of the soybean meal-based materials is attributable both to their higher electronic conductivity and improved ion diffusion through the porous structure (shorter Warburg region, i.e., lower EDR) owing to the presence of larger pores (see Figure 6c-d). When compared to the commercial activated carbon, both improved electronic conductivity and ion diffusion through the porous structure can be seen, the largest enhancement being recorded on ion diffusion. The ideal capacitive behavior of the materials is supported by the Bode plots in Figure 8b, which show a phase angle at low frequencies close to -90° . Furthermore, the time constant of the different materials, derived from the characteristic frequency f_0 at the phase angle of -45° , has a value in the range of 1.2–2.0 s (compared with 3.5 s for the commercial activated carbon), confirming the rapid diffusion of ions inside the structure of these materials. Furthermore, the robustness of the supercapacitors is evidenced by capacitance retentions of 94–97% after 10000 cycles at 5 A g^{-1} (see Figure S11a).

In order to increase the cell voltage and hence the amount of energy stored in the supercapacitor, as well as to enhance the environmental friendliness of the devices, Li_2SO_4 was tested as electrolyte. In this case, a stable 1.5 V cell voltage was obtained (see Figures S11b-c, proving a capacitance retention >90%), compared to 1 V in H_2SO_4 , owing to the higher overpotentials for oxygen and especially hydrogen evolution.^[22,52,53] However, the rate capability in this less conductive electrolyte was lower for all the materials tested, as can be seen in Figure 7b. The restricted ion diffusion is particularly marked in glucose-based materials due to their narrower PSDs (see Figure 6c), which can only work up to $10\text{--}20\text{ A g}^{-1}$. This is further supported by EIS (Figure 8c), which not only reveals a higher ESR in the neutral electrolyte compared to the acid one, but also a much greater resistance to the diffusion of ions. Likewise, the values of capacitance are lower than in H_2SO_4 ($\sim 150\text{--}160\text{ F g}^{-1}/33\text{--}74\text{ F cm}^{-3}$ at 0.2 A g^{-1}) probably due to the lower contribution of pseudocapacitive reactions in neutral electrolytes, but still well placed within the values of state-of-the-art carbons.^[22,54–57] Nevertheless, the higher cell voltage of Li_2SO_4 -based supercapacitors leads to an increase in the amount of energy stored of *ca.* 60% for a power density up to $\sim 5\text{ kW kg}^{-1}$, as evidenced by the Ragone plots in Figure 7d.

A further boost to cell voltage was achieved by using the ionic liquid EMImTFSI dissolved in AN, i.e., 3 V. Its stability was confirmed by charge/discharge cycling at 10 A g^{-1} , which led to capacitance retentions in the 90–95% range after 7500 cycles (see Figure S11d). In this electrolyte, as shown in Figure 7c, the rate capability is also lower than in H_2SO_4 (maximum discharge current of $\sim 30\text{ A g}^{-1}$, see CD profiles in Figure S12) as are the capacitance values ($140\text{--}160\text{ F g}^{-1}/34\text{--}72\text{ F cm}^{-3}$ at 0.2 A g^{-1}) owing to the limited or small contribution of pseudocapacitance by surface groups. This is evidenced in the Bode plots in Figure 8d, which show a much slower frequency response in EMImTFSI/AN and a phase angle at low frequencies that is

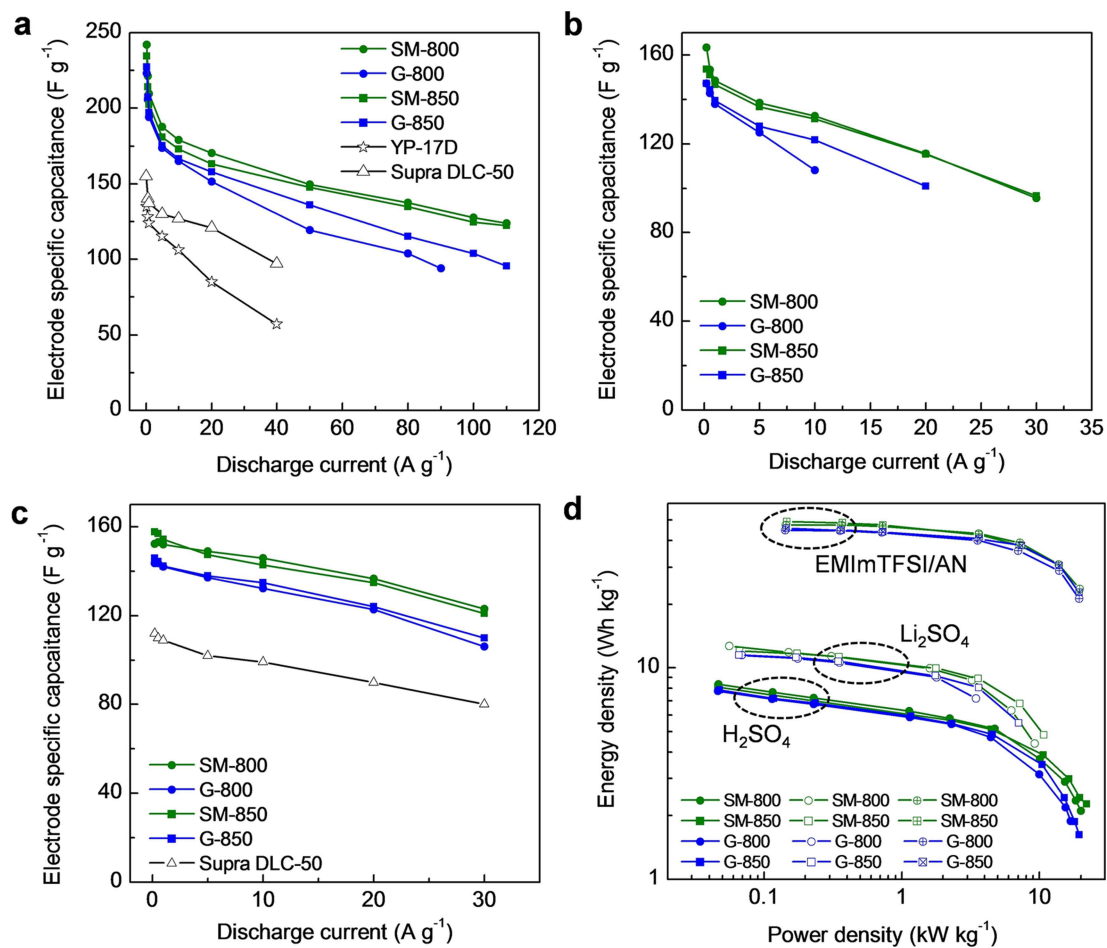


Figure 7. Electrochemical performance. Impact of discharge current density on electrode specific capacitance in a) 1 M H_2SO_4 , b) 1 M Li_2SO_4 , and c) EMImTFSI/AN, d) Ragone-like plots.

closer to -90° than that of the acid electrolyte. However, both capacitance and rate capability (>70% capacitance retention at 30 A g^{-1}) are still good for this kind of electrolyte when compared to the state-of-the-art carbons and commercial activated carbons, especially when using carbon loadings as high as 10 mg cm^{-2} (carbon loadings are normally around $1-2 \text{ mg cm}^{-2}$).^[44,58-60] As in the case of the acid electrolyte, the surface area normalized capacitance increases in line with the trend of microporosity, from $5.9 \mu\text{F cm}^{-2}$ for SM-850 to $7.4 \mu\text{F cm}^{-2}$ for G-800, in agreement with the greater efficiency with which micropores store ions. More importantly, the large voltage achieved with this electrolyte makes it possible to store as much as *ca.* 50 kWh kg^{-1} ($10-23 \text{ kWh L}^{-1}$) at low power density and still provide $22-23 \text{ kWh kg}^{-1}$ ($\sim 5-10 \text{ kWh L}^{-1}$) at a high power density of *ca.* 20 kWh kg^{-1} ($4-7 \text{ kW L}^{-1}$). These results highlight the versatility of these materials for use with a variety of electrolytes with different ionic conductivities, providing good energy and power density values owing to the easy accessibility to the micropores in this 3D structure, especially in the case of materials that also contain some mesopores.

3. Conclusions

In summary, we have developed a sustainable salt template-assisted chemical activation approach for the fabrication of 3D highly porous carbons. It is based on the use of low-toxic or non-toxic potassium salts as template (KCl and K_2CO_3) and activating agent (K_2CO_3), and of biomass-derivatives as carbon precursor (i.e., glucose and soybean meal). The self-assembly of all the compounds into a 3D structure was induced by freeze-drying. After carbonization ($800-850^\circ\text{C}$) and after being washed with water to eliminate the salts, a 3D porous carbon was obtained. These carbons possess BET surface areas in the $\sim 2000-2600 \text{ m}^2 \text{ g}^{-1}$ range and pore volumes of $0.8-1.4 \text{ cm}^3 \text{ g}^{-1}$, with most of their porosity corresponding to micropores (>70%). When tested as supercapacitor electrodes with commercial-level carbon electrode loadings, these materials provided an excellent rate capability independently of whether an aqueous (H_2SO_4 and Li_2SO_4) or an ionic liquid (EMImTFSI/AN) electrolyte was used due to the rapid access of the electrolyte ions to the micropores of this 3D architecture.

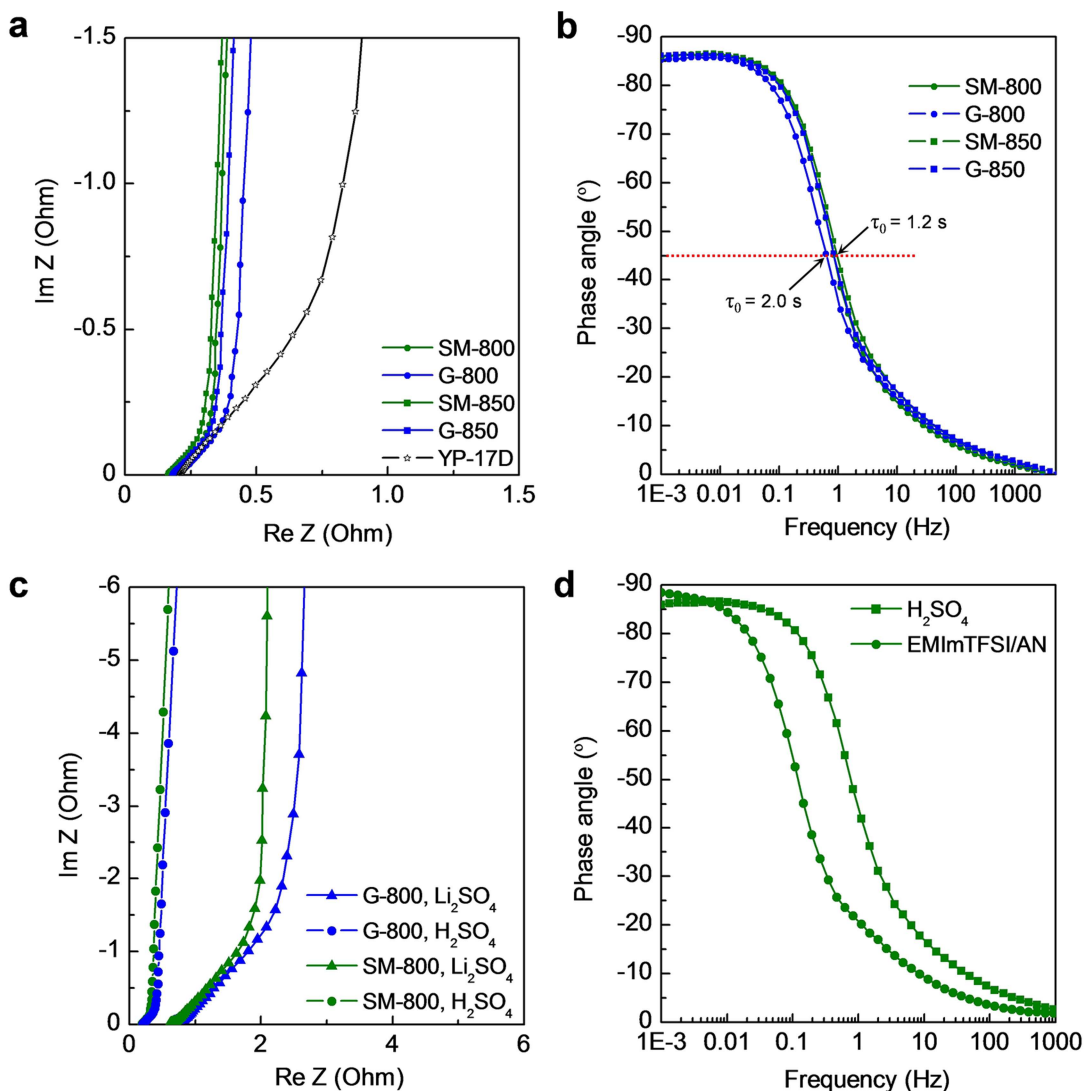


Figure 8. EIS study at OCV of the as-assembled supercapacitors. a) Nyquist and b) Bode plots in 1 M H_2SO_4 , c) comparison of the Nyquist plots in acid and neutral aqueous electrolyte for the porous carbons prepared at 800 °C and d) Bode plots for SM-850 in 1 M H_2SO_4 and EMImTFSI/AN.

Experimental Section

Synthesis of 3D Porous Carbons

α -D-Glucose (96%, Aldrich) and soybean meal (i.e., defatted soybean flour, see reference [61] for the defatting procedure) were used as carbon precursors. In a typical synthesis, potassium chloride (> 99.5%, Sigma Aldrich) was first dissolved in water, followed by potassium carbonate (Merck) and the carbon precursor, using a $\text{K}_2\text{CO}_3/\text{KCl}$ /carbon precursor weight ratio of 1/6.7/1. Afterwards, the mixture was frozen in liquid nitrogen (-196°C) and then transferred to a lyophilizer (Telstar Cryodos) and freeze-dried at a temperature of -50°C and at a pressure of 0.06 mbar. The solid thus obtained was heat-treated at $800\text{--}850^\circ\text{C}$ (3°C min^{-1}) under a nitrogen gas flow and held at this temperature for 1 h. The sample was washed several times with hot distilled water in order to remove any inorganic impurities. Finally, the solid product was dried in an oven at 120°C for 3 h. The carbons thus produced were labelled X-T, where X=G (glucose) and SM (soybean meal) and T=synthesis temperature. Carbon materials were also prepared from glucose and soybean meal using only potassium carbonate (K_2CO_3 /carbon precursor weight ratio=1/1) or potassium chloride (KCl/carbon precursor weight ratio=6.7/1). These carbons were denoted X-CK-800 when only K_2CO_3 was used, and X-K-800 when only potassium chloride was used. On the other hand, carbon materials were additionally prepared from glucose by using potassium oxalate as activating agent instead of potassium carbonate ($\text{K}_2\text{C}_2\text{O}_4$ /glucose weight ratio=1/1) and a mixture of potassium oxalate and KCl ($\text{K}_2\text{C}_2\text{O}_4/\text{KCl}$ /glucose = 1/6.7/1 weight ratio).

Scanning electron microscopy (SEM) images were recorded on a Quanta FEG650 (FEI) microscope, whereas the transmission electron microscopy (TEM) images were recorded on a JEOL (JEM 2100-F) apparatus operating at 200 kV. The nitrogen sorption isotherms of the carbon samples were measured at -196°C using a Micromeritics ASAP 2020 sorptometer. Prior to the measurement, the material was outgassed at 200°C for 1 h. The apparent surface area (S_{BET}) was calculated from the N_2 isotherms using the Brunauer-Emmett-Teller (BET) method.^[62,63] The total pore volume (V_p) was determined from the amount of nitrogen adsorbed at a relative pressure (p/p_0) of 0.95. The pore size distributions were determined

Physical and Chemical Characterization

Scanning electron microscopy (SEM) images were recorded on a Quanta FEG650 (FEI) microscope, whereas the transmission electron microscopy (TEM) images were recorded on a JEOL (JEM 2100-F) apparatus operating at 200 kV. The nitrogen sorption isotherms of the carbon samples were measured at -196°C using a Micromeritics ASAP 2020 sorptometer. Prior to the measurement, the material was outgassed at 200°C for 1 h. The apparent surface area (S_{BET}) was calculated from the N_2 isotherms using the Brunauer-Emmett-Teller (BET) method.^[62,63] The total pore volume (V_p) was determined from the amount of nitrogen adsorbed at a relative pressure (p/p_0) of 0.95. The pore size distributions were determined

by applying the Quenched-Solid Density Functional Theory (QSDFT) method to the nitrogen adsorption data and assuming a slit pore model. The micropore volume (V_{microp}) was obtained from the QSDFT PSD (volume of pores $< 2 \text{ nm}$). Elemental analysis (C, N and O) of the samples was carried out on a LECO CHN-932 microanalyzer. X-ray diffraction (XRD) patterns were obtained on a Siemens D5000 instrument operating at 40 kV and 20 mA and using a Cu K α radiation source ($\lambda = 0.15406 \text{ nm}$). Thermogravimetric analysis (TGA) curves were recorded on a TA Instruments Q6000 TGA system (3°C min^{-1} – 850°C under N_2). Temperature programmed desorption (TPD) experiments were performed on a Micromeritics Autochem II 2920 coupled to a Pfeiffer-Vacuum Omnistar quadrupole mass spectrometer (3°C min^{-1} – 900°C under Ar). The evolution of CO ($m/z = 28$), CO_2 ($m/z = 44$), H_2O ($m/z = 18$) and H_2 ($m/z = 2$) was recorded. To determine the dc electrical conductivity of the porous carbons, ~50 mg of each carbon was placed inside a hollow Nylon cylinder with an inner diameter of 8 mm and pressed in between two plungers under a pressure of 7.1 MPa.

Electrochemical Characterization

The electrodes consist of a mixture of 85 wt% of active material, 10 wt% of polytetrafluoroethylene (PTFE) binder (Aldrich, 60 wt% suspension in water) and 5% of Super C65 (Timcal). The electrochemical measurements were carried out in two-electrode Swagelok™ type cells in 1 M H_2SO_4 , 1 M Li_2SO_4 , and EMIMTSI/AN (1-Ethyl-3-methylimidazolium bis(trifluoromethylsulfonyl)imide, wt. ratio 1:1) (99%, Ionic Liquids Technology, Germany) electrolyte solutions. The supercapacitors were assembled using two carbon electrodes of comparable mass (carbon loading of $9\text{--}11 \text{ mg cm}^{-2}$, thickness $\sim 250\text{--}460 \mu\text{m}$ depending on the material), electrically isolated by glassy fibrous separators. Commercial activated carbons (Kuraray YP-17D and Norit Supra DLC-50) were also measured for comparison purposes. The electrochemical characterization was performed at room temperature using a computer-controlled potentiostat (Biologic VMP3 multichannel generator) and consisted of cyclic voltammetry experiments (CV), electrochemical impedance spectroscopy studies (EIS) and galvanostatic charge/discharge (CD) cycling tests. A complete description of the experiments performed, and the calculations can be found in the Supporting Information.

Acknowledgments

This research work was supported by the Spanish MINECO-FEDER (CTQ2015-63552-R) and regional GRUPIN2018 (IDI/2018/000148).

Conflict of Interest

The authors declare no conflict of interest.

Keywords: biomass • green synthesis • porous carbon • supercapacitor • template-assisted synthesis

- [1] L. Borchardt, M. Oschatz, S. Kaskel, *Mater. Horiz.* **2014**, *1*, 157–168.
- [2] L. L. Zhang, Y. Gu, X. S. Zhao, *J. Mater. Chem. A* **2013**, *1*, 9395–9408.
- [3] A. Ghosh, Y. H. Lee, *ChemSusChem* **2012**, *5*, 480–499.

- [4] M. A. Rahman, Y. C. Wong, G. Song, C. Wen, *J. Porous Mater.* **2015**, *22*, 1313–1343.
- [5] J.-G. Wang, K. Xie, B. Wei, *Nano Energy* **2015**, *15*, 413–444.
- [6] J. Jin, X. Tian, N. Srikanth, L. B. Kong, K. Zhou, *J. Mater. Chem. A* **2017**, *5*, 10110–10126.
- [7] H. Woo, J. Kang, J. Kim, C. Kim, S. Nam, B. Park, *Electron. Mater. Lett.* **2016**, *12*, 551–567.
- [8] M. Zhou, H.-L. Wang, S. Guo, *Chem. Soc. Rev.* **2016**, *45*, 1273–1307.
- [9] S. Sharma, B. G. Pollet, *J. Power Sources* **2012**, *208*, 96–119.
- [10] K. V. Kumar, K. Preuss, M.-M. Titirici, F. Rodríguez-Reinoso, *Chem. Rev.* **2017**, *117*, 1796–1825.
- [11] Y. Xia, Z. Yang, Y. Zhu, *J. Mater. Chem. A* **2013**, *1*, 9365–9381.
- [12] X.-Q. Zhang, W.-C. Li, A.-H. Lu, *New Carbon Mater.* **2015**, *30*, 481–501.
- [13] Y. Zhao, X. Liu, Y. Han, *RSC Adv.* **2015**, *5*, 30310–30330.
- [14] J. Deng, M. Li, Y. Wang, *Green Chem.* **2016**, *18*, 4824–4854.
- [15] H. Lu, X. S. Zhao, *Sust. Energy Fuels* **2017**, *1*, 1265–1281.
- [16] W. Tang, Y. Zhang, Y. Zhong, T. Shen, X. Wang, X. Xia, J. Tu, *Mater. Res. Bull.* **2017**, *88*, 234–241.
- [17] Z. Gao, Y. Zhang, N. Song, X. Li, *Mater. Res. Lett.* **2017**, *5*, 69–88.
- [18] J. Wang, S. Kaskel, *J. Mater. Chem.* **2012**, *22*, 23710–23725.
- [19] M. Sevilla, R. Mokaya, *Energy Environ. Sci.* **2014**, *7*, 1250–1280.
- [20] M. Sevilla, P. Valle-Vigón, A. B. Fuertes, *Adv. Funct. Mater.* **2011**, *21*, 2781–2787.
- [21] M.-H. Kim, S. Yun, H. S. Park, J. T. Han, K.-B. Kim, K. C. Roh, *J. Mater. Chem. A* **2015**, *3*, 2564–2567.
- [22] A. B. Fuertes, M. Sevilla, *ChemSusChem* **2015**, *8*, 1049–1057.
- [23] J. Sun, J. Niu, M. Liu, J. Ji, M. Dou, F. Wang, *Appl. Surf. Sci.* **2018**, *427*, 807–813.
- [24] J. Deng, T. Xiong, F. Xu, M. Li, C. Han, Y. Gong, H. Wang, Y. Wang, *Green Chem.* **2015**, *17*, 4053–4060.
- [25] S. Zhu, J. Li, C. He, N. Zhao, E. Liu, C. Shi, M. Zhang, *J. Mater. Chem. A* **2015**, *3*, 22266–22273.
- [26] S. Zhu, J. Li, L. Ma, L. Guo, Q. Li, C. He, E. Liu, F. He, C. Shi, N. Zhao, *ACS Appl. Mater. Interfaces* **2016**, *8*, 11720–11728.
- [27] W. Qian, J. Zhu, Y. Zhang, X. Wu, F. Yan, *Small* **2015**, *11*, 4959–4969.
- [28] F. Pan, Y. Duan, A. Liang, J. Zhang, Y. Li, *Electrochim. Acta* **2017**, *238*, 375–383.
- [29] S. Zhu, J. Li, Q. Li, C. He, E. Liu, F. He, C. Shi, N. Zhao, *Electrochim. Acta* **2016**, *212*, 621–629.
- [30] W. Niu, L. Li, N. Wang, S. Zeng, J. Liu, D. Zhao, S. Chen, *J. Mater. Chem. A* **2016**, *4*, 10820–10827.
- [31] Z. Wang, S. Luo, F. Chen, D. Wang, Y. Liu, X. Qi, C. Shi, N. Zhao, *RSC Adv.* **2016**, *6*, 54718–54726.
- [32] C. He, S. Wu, N. Zhao, C. Shi, E. Liu, J. Li, *ACS Nano* **2013**, *7*, 4459–4469.
- [33] L. Chen, Z. Wang, C. He, N. Zhao, C. Shi, E. Liu, J. Li, *ACS Appl. Mater. Interfaces* **2013**, *5*, 9537–9545.
- [34] J. Chmiola, G. Yushin, Y. Gogotsi, C. Portet, P. Simon, P. L. Taberna, *Science* **2006**, *313*, 1760–1763.
- [35] N. Fechner, T.-P. Fellinger, M. Antonietti, *Adv. Mater.* **2013**, *25*, 75–79.
- [36] J. Pampel, T. P. Fellinger, *Adv. Energy Mater.* **2016**, *6*, 8.
- [37] J. Pampel, C. Denton, T.-P. Fellinger, *Carbon* **2016**, *107*, 288–296.
- [38] D. W. McKee, *Fuel* **1983**, *62*, 170–175.
- [39] J. I. Hayashi, T. Horikawa, I. Takeda, K. Muroyama, F. Nasir Ani, *Carbon* **2002**, *40*, 2381–2386.
- [40] J. Kopyscinski, M. Rahman, R. Gupta, C. A. Mims, J. M. Hill, *Fuel* **2014**, *117*, 1181–1189.
- [41] M. Sevilla, G. A. Ferrero, A. B. Fuertes, *Chem. Mater.* **2017**, *29*, 6900–6907.
- [42] J. Lee, J. Kim, T. Hyeon, *Adv. Mater.* **2006**, *18*, 2073–2094.
- [43] H. Shang, Y. Lu, F. Zhao, C. Chao, B. Zhang, H. Zhang, *RSC Adv.* **2015**, *5*, 75728–75734.
- [44] M. Sevilla, G. A. Ferrero, A. B. Fuertes, *Carbon* **2017**, *114*, 50–58.
- [45] B. Adeniran, E. Masika, R. Mokaya, *J. Mater. Chem. A* **2014**, *2*, 14696–14710.
- [46] M. Thommes, K. Kaneko, A. V. Neimark, J. P. Olivier, F. Rodriguez-Reinoso, J. Rouquerol, K. S. Sing, *Pure Appl. Chem.* **2015**, *87*, 1051–1069.
- [47] http://www.factsage.cn/fact/phase_diagram.php?file=KCl-K2CO3.jpg&dir=FTsalt.
- [48] J. Yaokawa, K. Oikawa, K. Anzai, *Calphad* **2007**, *31*, 155–163.
- [49] M. Sevilla, N. Diez, G. A. Ferrero, A. B. Fuertes, *Energy Storage Mater.* **2019**.
- [50] Y. Zhang, Q. Ma, H. Li, Y.-W. Yang, J. Luo, *Small* **2018**, *14*, 1800133.
- [51] B. E. Conway, *Electrochemical Supercapacitors, Scientific Fundamentals and Technological Applications*, 1999.

- [52] M. P. Bichat, E. Raymundo-Piñero, F. Béguin, *Carbon* **2010**, *48*, 4351–4361.
- [53] Q. Gao, L. Demarconnay, E. Raymundo-Pinero, F. Beguin, *Energy Environ. Sci.* **2012**, *5*, 9611–9617.
- [54] W. Gu, M. Sevilla, A. Magasinski, A. B. Fuertes, G. Yushin, *Energy Environ. Sci.* **2013**, *6*, 2465–2476.
- [55] M. Oschätz, S. Boukhalfa, W. Nickel, J. P. Hofmann, C. Fischer, G. Yushin, S. Kaskel, *Carbon* **2017**, *113*, 283–291.
- [56] Y. An, Z. Li, Y. Yang, B. Guo, Z. Zhang, H. Wu, Z. Hu, *Adv. Mater. Interfaces* **2017**, *4*, 1700033.
- [57] C. Schneidermann, N. Jäckel, S. Oswald, L. Giebel, V. Presser, L. Borchardt, *ChemSusChem* **2017**, *10*, 2416–2424.
- [58] Q.-L. Zhu, P. Pachfule, P. Strubel, Z. Li, R. Zou, Z. Liu, S. Kaskel, Q. Xu, *Energy Storage Mater.* **2018**, *13*, 72–79.
- [59] Y. Xu, Z. Lin, X. Zhong, X. Huang, N. O. Weiss, Y. Huang, X. Duan, *Nat Commun* **2014**, *5*.
- [60] Y. Zhu, S. Murali, M. D. Stoller, K. J. Ganesh, W. Cai, P. J. Ferreira, A. Pirkle, R. M. Wallace, K. A. Cychosz, M. Thommes, D. Su, E. A. Stach, R. S. Ruoff, *Science* **2011**, *332*, 1537–1541.
- [61] G. A. Ferrero, A. B. Fuertes, M. Sevilla, *Sci. Rep.* **2015**, *5*, 16618.
- [62] D. ISO, Determination of the Specific Surface Area of Solids by Gas Adsorption using the BET Method, German Institute of Normalization (DIN) **1995**, 1–19.
- [63] F. Rouquerol, J. Rouquerol, K. Sing, *Adsorption by powders and porous solids: principles, methodology and applications*, Academic Press, San Diego **1999**.

Manuscript received: March 13, 2019

Revised manuscript received: April 24, 2019

Accepted article published: April 24, 2019

Version of record online: May 7, 2019